

DISCRETE LATTICE BGK BOLTZMANN EQUATION COMPUTATIONS OF TRANSIENT INCOMPRESSIBLE TURBULENT JETS

KANNAN N. PREMNATH

*Maurice J. Zucrow Labs., School of Mechanical Engineering
Purdue University, West Lafayette, Indiana 47907, USA
E-mail: nandha@ecn.purdue.edu*

JOHN ABRAHAM

*Maurice J. Zucrow Labs., School of Mechanical Engineering
Purdue University, West Lafayette, Indiana 47907, USA
E-mail: jabraham@ecn.purdue.edu*

Received (received date)

Revised (revised date)

In this paper, computations of transient, incompressible, turbulent, plane jets using the discrete lattice BGK Boltzmann equation are reported. *A priori* derivation of the discrete lattice BGK Boltzmann equation with a spatially and temporally dependent relaxation time parameter, which is used to represent the averaged flow field, from its corresponding continuous form is given. The averaged behavior of the turbulence field is represented by the standard k - ϵ turbulence model and computed using a finite-volume scheme on non-uniform grids. Computed results are compared with analytical solutions, experimental data and results of other computational methods. Satisfactory agreement is shown.

Keywords: Lattice Boltzmann Method; Turbulence Modeling; Non-uniform Grids; Finite Volume Methods; Turbulent Jets

1. Introduction

The computational method based on the lattice Boltzmann equation (LBE) is relatively new for fluid dynamics. It is part of the paradigm of simulating complex physical phenomena, in particular fluid flows, that are based on the observation that the interactions of quasi-particles represented by simple models could give rise to very complex emergent phenomena. In 1986, in the seminal works of Frisch, Hasslacher and Pomeau¹ and Wolfram², the lattice gas automaton (LGA) was introduced to simulate the fluid behavior described by the Navier-Stokes equations. Their work showed that the key to recovering hydrodynamics from such models is that the underlying lattice structure, in which the particles are constrained to move and collide while obeying mass and momentum conservation laws, satisfy certain symmetry properties. The lattice Boltzmann equation (LBE) was introduced by MacNamara and Zanetti³ to overcome certain drawbacks of the LGA such as the

presence of statistical noise and the lack of Galilean invariance. A number of refinements were made, such as the simplification of the description of the collision of particle populations^{4,5} by means of the well-known Bhatnagar-Gross-Krook (BGK) model⁶ which resulted in a considerable simplification of the LBE. In the above sense, in which the LBE represents the stream-and-collide picture of the particle populations, it may be essentially considered as an extension of the LGA.

On the other hand, it was believed that the LBE could also be connected to the Boltzmann equation, a well known kinetic equation in non-equilibrium statistical mechanics, that describes the evolution of the particle populations in terms of the distribution functions. It was formally shown that the LBE can be derived *á priori* from the Boltzmann equation when its continuous velocity space is considerably simplified to a certain discrete velocity space⁷⁻⁹. With the foundations of the kinetic theory, many ideas pertinent to the Boltzmann equation have been extended to the LBE or the discrete lattice BGK Boltzmann equation. The rapid development and the applications of the lattice Boltzmann method (LBM) that involves the solution of the LBE has been documented in several review papers¹⁰⁻¹⁴ and monographs^{15,16}. In particular, the ability of the method to model physics at a smaller scale makes it a potentially promising tool to simulate fluid flows involving interfaces such as multiphase and multicomponent flows and other complex flows. Algorithmically, the method involves operations that are explicit and local and hence naturally amenable for implementation on almost all types of parallel computers. Moreover, in the case of incompressible flows, conventional computational methods typically require the solution of a Poisson-type equation for the computation of pressure field^{17,18} which may be time consuming and only partly parallelizable¹⁹; on the other hand, the pressure is always computed locally through an equation of state in the LBM.

Ever since the beginning of the development of the LGA, the precursor to the LBE, there were speculations²⁰ about its application to the simulation of turbulence, the most dominant form of fluid flow that occurs in nature as well as engineering applications. Because of the inherent limitations of the LGA, some of which were discussed earlier, it was noted that its computational requirements would be far more demanding than that of conventional macroscopic methods. However, with the introduction of the LBE, with its physical as well as computational advantages, direct computation of turbulence based on the LBE became feasible. Martinez *et al.*²¹ computed decaying turbulence in a shear layer and assessed the accuracy of the LBE by comparison of its results with results obtained by employing the spectral method. It was shown that the LBE is almost as fast as the spectral method on a serial computer and that it may well be more efficient if parallel computing strategies are utilized. Some notable work using the LBE aimed at understanding the physics of turbulence are the studies on the enstrophy cascade range²² and the energy inverse cascade range¹¹ in two-dimensional forced turbulence, the study of generalized extended self-similarity in three-dimensional, inhomogeneous shear turbulence²³ and the work on three-dimensional turbulent channel flow²⁴. It is

interesting to note that there has been a growing interest in the use of kinetic theory based approaches involving certain other forms of the Boltzmann equation to represent turbulence^{25,26}. While such studies, where the LBE or some other forms of the Boltzmann equation were used to resolve all the length and time scales, are important from a fundamental point of view, for high-Reynolds number flows of engineering interest some form of modeling within the LBE framework is desirable.

Turbulence modeling efforts within the LBE framework are being pursued through two approaches: (i) modeling based on the strict kinetic-theoretic formulations; and, (ii) modeling based on traditional concepts for which extensive literature already exist. The first approach is a more recent one that involves the application of the renormalization group (RG) analysis to the simplified form of the Boltzmann equation, such as the LBE, to develop a model for turbulence²⁷. It was found that this introduces *low Knudsen regime closure*, a feature that is peculiar to the kinetic equation, which the authors believe could potentially offer new physical insights as well as alternative mathematical treatments when compared to the Navier-Stokes equations. As this approach is still in its early stages, much work remains to be done. While the issues related to the first approach continue to be addressed, it is important to develop practical turbulence models for the LBE so that flows of practical interest can be computed within the LBE framework. In this respect, traditional, statistical averaged procedures to turbulence modeling have been extended to the LBE^{28–30}. Essentially, in this second approach, the relaxation time parameter that appear in the BGK model for the collision term in the LBE is now considered to be a *spatially and temporally dependent variable*, instead of a constant. As a result, the expression for viscosity that can be obtained from the Chapman-Enskog multiscale expansion³¹ can be considered to be the sum of the laminar viscosity of the fluid and a spatially and temporally dependent eddy viscosity, which can be modeled using any statistical averaged approach. An interesting question is whether we can derive this discrete lattice BGK Boltzmann equation with spatially and temporally dependent relaxation time parameter *a priori* from its corresponding continuous form. In the next section, we address this question.

It is important to assess the accuracy of the LBE used in conjunction with a turbulence model for flows of practical interest. Recently, it has been used to compute turbulent flow over an airfoil³². In this paper, we consider another application, namely, the computation of turbulent jets. Fluid jets are encountered in many engineering applications such as internal combustion engines, gas turbine combustors, industrial spray systems and a variety of other situations. Such flows are almost exclusively turbulent, with Reynolds number, Re , of the order of 10^5 or greater. Understanding the transient process of mixing is important in such situations. Direct simulations of jets would be limited to relatively low Reynolds numbers, of the order of few thousands. Hence it becomes imperative to use a model to represent turbulence and thereby compute its effect on the resolved flow field. In this work, we use the standard $k-\epsilon$ turbulence model³³ in conjunction with the LBE, such that the latter would represent the unsteady, mean flow field behavior, to study transient

incompressible plane jets. The time-marching nature of LBM is naturally beneficial for this problem that is inherently transient in nature.

The rest of the paper is organized as follows: In the next section, i.e. Section 2, an *á priori* derivation of the discrete lattice BGK Boltzmann equation, with a spatially and temporally dependent relaxation time, from its continuous version is provided. The analysis is an extension of that provided in works of He and Luo^{7,8}. In Section 3, the LBE as applied to simulate incompressible flows is discussed. As it has been shown that adequate resolution is important to study jets³⁴, it is necessary to employ non-uniform lattice grids within the LBE framework. Hence the LBE extension to non-uniform lattice grids is subsequently described in Section 4. This is followed by a discussion in Section 5 on the representation of turbulence within the LBE framework. The hybrid numerical scheme for the solution of the LBE and turbulence model and the computational conditions for the turbulent jet are described in Sections 6 and 7 respectively. In Section 8, the computed results are compared with analytical solutions, measurements, and published results from other computational methods. Finally, the paper closes with summary and conclusions in Section 9.

2. Analysis

Consider the Boltzmann equation with the BGK form for the collision term, where the relaxation time parameter is taken to be a spatially and temporally dependent variable

$$\frac{\partial f}{\partial t} + \boldsymbol{\xi} \cdot \nabla f = -\frac{1}{\lambda(\mathbf{x}, t)} (f - f^{eq}). \quad (1)$$

Here $f(\mathbf{x}, \boldsymbol{\xi}, t)$ is the single-particle distribution function, $\boldsymbol{\xi}$ is the particle velocity, $\lambda(\mathbf{x}, t)$ is the spatially and temporally dependent relaxation time, and f^{eq} is the local Maxwellian given by

$$f^{eq} = \frac{\rho}{(2\pi RT)^{D/2}} \exp \left[-\frac{(\boldsymbol{\xi} - \mathbf{u})^2}{2RT} \right], \quad (2)$$

where R is the ideal gas constant, D is the dimension of the space, and ρ , \mathbf{u} and T are the *mean* fluid density, velocity and temperature respectively. Limiting ourselves to the case of isothermal flows, the fluid density and velocity are obtained as the kinetic moments of the distribution function, i.e.

$$\rho = \int f d\boldsymbol{\xi} = \int f^{eq} d\boldsymbol{\xi}, \quad (3)$$

$$\rho \mathbf{u} = \int \boldsymbol{\xi} f d\boldsymbol{\xi} = \int \boldsymbol{\xi} f^{eq} d\boldsymbol{\xi}. \quad (4)$$

Equation (1) can be formally written in the form of an inhomogeneous ordinary differential equation with variable coefficients

$$\frac{df}{dt} + \frac{1}{\lambda(\mathbf{x}, t)} f = \frac{1}{\lambda(\mathbf{x}, t)} f^{eq}, \quad (5)$$

where $\frac{d}{dt} = \frac{\partial}{\partial t} + \boldsymbol{\xi} \cdot \nabla$ is the streaming operator or the time derivative operator along the characteristic direction $\boldsymbol{\xi}$. The above equation can be formally integrated over a time step of δ_t , i.e.

$$\begin{aligned} f(\mathbf{x} + \boldsymbol{\xi}\delta_t, \boldsymbol{\xi}, t + \delta_t) &= e^{-\int_0^{\delta_t} \frac{dt'}{\lambda(\mathbf{x} + \boldsymbol{\xi}t', t + t')}} \\ &\times \int_0^{\delta_t} e^{\int_0^{\delta_t} \frac{ds}{\lambda(\mathbf{x} + \boldsymbol{\xi}s, t + s)}} \frac{1}{\lambda(\mathbf{x} + \boldsymbol{\xi}t', t + t')} f^{eq}(\mathbf{x} + \boldsymbol{\xi}t', \boldsymbol{\xi}, t + t') dt' \\ &+ e^{-\int_0^{\delta_t} \frac{dt'}{\lambda(\mathbf{x} + \boldsymbol{\xi}t', t + t')}} f(\mathbf{x}, \boldsymbol{\xi}, t), \end{aligned} \quad (6)$$

where $s, t' \in [0, \delta_t]$. Assuming that δ_t is small enough and the equilibrium distribution function, f^{eq} , and the relaxation time parameter, λ , are locally smooth functions, the following linear approximation by Taylor expansion may be made:

$$f^{eq}(\mathbf{x} + \boldsymbol{\xi}t', \boldsymbol{\xi}, t + t') = G_1 + G_{21}t' + O(\delta_t^2), \quad (7)$$

$$\lambda(\mathbf{x} + \boldsymbol{\xi}t', t + t') = \Lambda_1 + \Lambda_{21}t' + O(\delta_t^2), \quad (8)$$

where

$$\begin{aligned} G_1 &= f^{eq}(\mathbf{x}, \boldsymbol{\xi}, t), \quad G_{21} = \frac{f^{eq}(\mathbf{x} + \boldsymbol{\xi}\delta_t, \boldsymbol{\xi}, t + \delta_t) - f^{eq}(\mathbf{x}, \boldsymbol{\xi}, t)}{\delta_t}, \\ \Lambda_1 &= \lambda(\mathbf{x}, t), \quad \Lambda_{21} = \frac{\lambda(\mathbf{x} + \boldsymbol{\xi}\delta_t, t + \delta_t) - \lambda(\mathbf{x}, t)}{\delta_t}. \end{aligned}$$

In the above, and in what follows, considering only first order accurate approximations in time^{7,8}, the leading terms of the order of $O(\delta_t^2)$ are neglected. Hence, the following approximation in the integrand in Eq. (6) may be made:

$$\begin{aligned} \frac{1}{\lambda(\mathbf{x} + \boldsymbol{\xi}t', t + t')} &= \frac{1}{\Lambda_1 \left(1 + \frac{\Lambda_{21}}{\Lambda_1}t'\right)} = \frac{1}{\Lambda_1} \left(1 - \frac{\Lambda_{21}}{\Lambda_1}t'\right) + O(\delta_t^2), \\ \frac{1}{\lambda(\mathbf{x} + \boldsymbol{\xi}t', t + t')} f^{eq}(\mathbf{x} + \boldsymbol{\xi}t', \boldsymbol{\xi}, t + t') &= \frac{G_1 + G_{21}t'}{\Lambda_1 + \Lambda_{21}t'} = \frac{1}{\Lambda_1} G_1 + \Lambda_1 \left(G_1 - \frac{\Lambda_{21}}{\Lambda_1}\right) t' + O(\delta_t^2), \\ e^{\int_0^{t'} \frac{ds}{\lambda(\mathbf{x} + \boldsymbol{\xi}s, t + s)}} &= e^{\int_0^{t'} \frac{1}{\Lambda_1} \left(1 - \frac{\Lambda_{21}}{\Lambda_1}s\right) ds} \approx e^{\frac{t'}{\Lambda_1}}. \end{aligned}$$

Substituting the above in Eq. (6), we get

$$\begin{aligned} f(\mathbf{x} + \boldsymbol{\xi}\delta_t, \boldsymbol{\xi}, t + \delta_t) &= e^{-\frac{\delta_t}{\Lambda_1}} \int_0^{\delta_t} e^{\frac{t'}{\Lambda_1}} \left[\frac{1}{\Lambda_1} G_1 + \frac{1}{\Lambda_1} \left(G_1 - \frac{\Lambda_{21}}{\Lambda_1}\right) t' \right] dt' \\ &+ e^{-\frac{\delta_t}{\Lambda_1}} f(\mathbf{x}, \boldsymbol{\xi}, t). \end{aligned} \quad (9)$$

Now, as

$$\int_0^{\delta_t} e^{\frac{t'}{\Lambda_1}} dt' = \Lambda_1 \left(e^{\frac{\delta_t}{\Lambda_1}} - 1\right), \quad \int_0^{\delta_t} t' e^{\frac{t'}{\Lambda_1}} dt' = \Lambda_1 \left[\delta_t e^{\frac{\delta_t}{\Lambda_1}} - \Lambda_1 \left(e^{\frac{\delta_t}{\Lambda_1}} - 1\right)\right],$$

we can rewrite Eq. (9) as follows:

$$\begin{aligned}
 & f(\mathbf{x} + \boldsymbol{\xi}\delta_t, \boldsymbol{\xi}, t + \delta_t) \\
 = & e^{-\frac{\delta_t}{\Lambda_1}} \left\{ \frac{1}{\Lambda_1} G_1 \left[\Lambda_1 \left(e^{\frac{\delta_t}{\Lambda_1}} - 1 \right) \right] + \frac{1}{\Lambda_1} \left(G_1 - \frac{\Lambda_{21}}{\Lambda_1} \right) \left[\Lambda_1 \left\{ \delta_t e^{\frac{\delta_t}{\Lambda_1}} - \Lambda_1 \left(e^{\frac{\delta_t}{\Lambda_1}} - 1 \right) \right\} \right] \right\} \\
 & + e^{-\frac{\delta_t}{\Lambda_1}} f(\mathbf{x}, \boldsymbol{\xi}, t). \tag{10}
 \end{aligned}$$

Employing Taylor expansion we get $e^{\pm\frac{\delta_t}{\Lambda_1}} = 1 \pm \frac{\delta_t}{\Lambda_1} + O(\delta_t^2)$. Substituting this in the above equation

$$\begin{aligned}
 f(\mathbf{x} + \boldsymbol{\xi}\delta_t, \boldsymbol{\xi}, t + \delta_t) &= \left(1 - \frac{\delta_t}{\Lambda_1} \right) \left[G_1 \left(\frac{\delta_t}{\Lambda_1} \right) + \frac{1}{\Lambda_1} \left(G_1 - \frac{\Lambda_{21}}{\Lambda_1} \right) \left(\frac{\delta_t^2}{\Lambda_1} \right) \right] \\
 &+ \left(1 - \frac{\delta_t}{\Lambda_1} \right) f(\mathbf{x}, \boldsymbol{\xi}, t), \tag{11}
 \end{aligned}$$

and neglecting terms of the order of $O(\delta_t^2)$

$$f(\mathbf{x} + \boldsymbol{\xi}\delta_t, \boldsymbol{\xi}, t + \delta_t) = \frac{\delta_t}{\Lambda_1} G_1 + \left(1 - \frac{\delta_t}{\Lambda_1} \right) f(\mathbf{x}, \boldsymbol{\xi}, t), \tag{12}$$

or, finally we obtain the time-discrete version of the Boltzmann equation

$$f(\mathbf{x} + \boldsymbol{\xi}\delta_t, \boldsymbol{\xi}, t + \delta_t) - f(\mathbf{x}, \boldsymbol{\xi}, t) = -\frac{1}{\tau(\mathbf{x}, t)} [f(\mathbf{x}, \boldsymbol{\xi}, t) - f^{eq}(\mathbf{x}, \boldsymbol{\xi}, t)], \tag{13}$$

where $\tau(\mathbf{x}, t) = \lambda(\mathbf{x}, t) / \delta_t$. As shown by He and Luo^{7,8}, the equilibrium distribution function may be represented by a truncated small velocity expansion and the phase space is discretized such that the numerical quadrature that is used in the calculation of the kinetic moments for the conserved variables is exact. Thus, for example, in the case of the two-dimensional, nine-velocity (D2Q9) model⁴, shown in Fig. 1, the numerical quadrature naturally corresponds to the third-order Gauss-Hermite quadrature. Hence, Eqs. (2-4) and (13) may be written in discretized form as

$$f_\alpha(\mathbf{x} + \mathbf{e}_\alpha\delta_t, t + \delta_t) - f_\alpha(\mathbf{x}, t) = -\frac{1}{\tau(\mathbf{x}, t)} [f_\alpha(\mathbf{x}, t) - f_\alpha^{eq}(\mathbf{x}, t)], \tag{14}$$

$$\rho = \sum_\alpha f_\alpha(\mathbf{x}, t) = \sum_\alpha f_\alpha^{eq}(\mathbf{x}, t), \tag{15}$$

$$\rho \mathbf{u} = \sum_\alpha f_\alpha(\mathbf{x}, t) \mathbf{e}_\alpha = \sum_\alpha f_\alpha^{eq}(\mathbf{x}, t) \mathbf{e}_\alpha, \tag{16}$$

$$f_\alpha^{eq} = w_\alpha \rho \left[1 + \frac{3}{c^2} (\mathbf{e}_\alpha \cdot \mathbf{u}) + \frac{9}{2c^4} (\mathbf{e}_\alpha \cdot \mathbf{u})^2 - \frac{3}{2c^2} u^2 \right], \tag{17}$$

where

$$w_\alpha = \begin{cases} 4/9 & \alpha = 0 \\ 1/9 & \alpha = 1, 2, 3, 4 \\ 1/36 & \alpha = 5, 6, 7, 8 \end{cases}$$

and \mathbf{e}_α is the discrete set of the velocity space of $\boldsymbol{\xi}$ shown in Fig. 1, with the Cartesian component of speed given by $c = \delta_x/\delta_t$ where δ_x is the lattice spacing and α is the velocity direction. Also, $f_\alpha(\mathbf{x}, t) = w_\alpha f_\alpha(\mathbf{x}, \mathbf{e}_\alpha, t)$, $f_\alpha^{eq}(\mathbf{x}, t) = w_\alpha f_\alpha^{eq}(\mathbf{x}, \mathbf{e}_\alpha, t)$. Thus, the discrete lattice BGK Boltzmann equation with spatially and temporally dependent relaxation time parameter, similar to the standard discrete lattice BGK Boltzmann equation with constant relaxation time parameter, follows *a priori* from its corresponding continuous version and is independent of the LGA. It can be shown using the Chapman-Enskog multiscale expansion^{12,31} that in the long-wavelength limit, the mean density and velocity obey the unsteady Reynolds averaged Navier-Stokes (RANS) equations with the viscosity related to the lattice parameters, i.e.

$$\nu(\mathbf{x}, t) = \nu_{\text{lam}} + \nu_{\text{eddy}}(\mathbf{x}, t) = \frac{1}{3}c^2 \left(\tau(\mathbf{x}, t) - \frac{1}{2} \right) \delta_t, \quad (18)$$

where ν_{lam} is the kinematic viscosity of the fluid and $\nu_{\text{eddy}}(\mathbf{x}, t)$ is the eddy viscosity which models the effect of turbulence on the flow field; The calculation of eddy viscosity is discussed in Section 5. In addition, it can be shown that the pressure is related to density by means of an equation of state

$$p(\mathbf{x}, t) = c_s^2 \rho(\mathbf{x}, t), \quad (19)$$

where c_s is the speed of sound, which is equal to $c/\sqrt{3}$.

3. The Incompressible Model

It may be noted that the LBE as discussed above always simulates the *weakly compressible* RANS equations which is valid for small Mach numbers, Ma . This is because of the fact that it models physics *locally*. Although true incompressibility, which amounts to infinite speed of sound, cannot be achieved in this model, it can be modified such that it minimizes the compressibility effects to approximately represent incompressible flows. In this work, we employ the “incompressible” LBE model³⁵. According to this model, to approximately represent incompressible flows with a constant density ρ_0 , terms of the order of $o(Ma^2)$ in the formulation of the LBE are systematically eliminated. This leads to a re-definition of the equilibrium distribution function, Eq. (17) and a modified expression for the calculation of fluid velocity $\rho_0 \mathbf{u} = \sum_\alpha f_\alpha \mathbf{e}_\alpha$. We use the modified equilibrium distribution function as derived by He and Luo³⁵:

$$f_\alpha^{eq} = w_\alpha \left[\rho + \rho_0 \left\{ \frac{3}{c^2} (\mathbf{e}_\alpha \cdot \mathbf{u}) + \frac{9}{2c^4} (\mathbf{e}_\alpha \cdot \mathbf{u})^2 - \frac{3}{2c^2} u^2 \right\} \right], \quad (20)$$

where the coefficient w_α is the same as that used in Eq. (17). In the literature, the LBE that results from these modifications is referred to as the “incompressible” LBE model.

4. Non-uniform Lattice Grids

The use of non-uniform lattice grids is desirable in many applications and is important in the simulation of jets where sharp gradients necessitate the use of high resolution in the near-orifice region³⁴. The original LBM is restricted to uniform grids, in that the minimum streaming distance of the particle populations in one time step is exactly equal to the minimum lattice spacing. In other words, the discretization of the configuration and particle velocity spaces are coupled. This lockstep advection of particle population is a feature inherited from the LGA and is not necessary for the LBE. Since the LBE is actually a simplified form of the Boltzmann equation which can be solved without the coupling of the physical and the particle velocity spaces, it can be solved on any mesh. Thus, it was proposed by He *et al.*³⁶ that the collisions still take place on the lattice grids in the manner discussed in the previous section; after collisions, the particle populations move according to their velocities \mathbf{e}_α ; although the advected distance of the particle populations may not, in general, coincide with the mesh spacing, the distribution functions in these locations can always be computed using *interpolation*; after interpolation, the collision and the streaming steps are repeated. It has been shown that, if the interpolation method is at least of second order, the Navier-Stokes equations can still be recovered from the LBE³⁷.

In this paper, we employ a second order Lagrange interpolation scheme to implement this interpolation-supplemented LBE. Figure 2 illustrates the use of this method on a stretched non-uniform lattice mesh. For example, for the particle velocity direction $\alpha = 1$, at locations (i, j) which corresponds to the lattice site A , $(i - 1, j)$ and $(i - 2, j)$, the collision step is first computed. Then, the particle populations from these locations stream in the positive i direction to a distance $|\mathbf{e}_\alpha| \delta_t$, which may not, in general, be equal to the local mesh spacing. After streaming, the distribution functions from these three new locations are interpolated to obtain the value of the distribution at the location A . For direction $\alpha = 3$, the lattice site locations are taken from the negative i direction as indicated at site B in the figure. A similar procedure is adopted for the other particle directions. With this arrangement, the incompressible LBE model is used to simulate jets.

5. Turbulence Modeling

The standard two-equation $k-\epsilon$ turbulence model is employed to represent the effects of the length and time scales in the turbulent flow. It was suggested earlier by Succi *et al.*²⁸ that these equations might be solved within the LBE framework by creating two additional populations, with components in the same directions as the particle distribution for each of the two scalar fields. An alternative approach is to solve the $k-\epsilon$ equations using entirely different computational grids with an appropriate numerical scheme³⁰. Here, we consider this latter approach to model the unresolved length and time scales in the turbulent, plane jets. The equations for the turbulent

kinetic energy, k and the dissipation rate, ϵ are given by

$$\rho_0 \left(\frac{\partial k}{\partial t} + \mathbf{u} \cdot \nabla k \right) = \frac{\partial}{\partial x_j} \left[\left(\mu_{\text{lam}} + \frac{\mu_T}{\sigma_k} \right) \frac{\partial k}{\partial x_j} \right] + \tau_{ij} S_{ij} - \rho_0 \epsilon, \quad (21)$$

$$\rho_0 \left(\frac{\partial \epsilon}{\partial t} + \mathbf{u} \cdot \nabla \epsilon \right) = \frac{\partial}{\partial x_j} \left[\left(\mu_{\text{lam}} + \frac{\mu_T}{\sigma_\epsilon} \right) \frac{\partial \epsilon}{\partial x_j} \right] + C_{\epsilon_1} \frac{\epsilon}{k} \tau_{ij} S_{ij} - C_{\epsilon_2} \rho_0 \frac{\epsilon^2}{k}. \quad (22)$$

The Reynolds stress and strain rate tensors, τ_{ij} and S_{ij} respectively, are related by the linear constitutive relation through the Bousinessq approximation

$$\tau_{ij} = 2\mu_T S_{ij} - 2/3\rho_0 k \delta_{ij}, \quad (23)$$

and the eddy viscosity is given by

$$\nu_{\text{eddy}}(\mathbf{x}, t) = \nu_T = \frac{\mu_T}{\rho_0} = C_\mu \frac{k^2}{\epsilon}. \quad (24)$$

The values of the model coefficients, $C_{\epsilon_1}, C_{\epsilon_2}, \sigma_k, \sigma_\epsilon, C_\mu$ used in this work are the same as that provided in Launder and Spalding³⁸. The strain rate tensor is directly computed from the second kinetic moment of the non-equilibrium part of the distribution function, without taking recourse to the finite-differencing of the velocity field, using

$$S_{ij} = -\frac{3}{2} \frac{1}{\delta_t} \frac{1}{\tau(\mathbf{x}, t)} \sum_\alpha \frac{e_{\alpha i} e_{\alpha j}}{c^2} \frac{(f_\alpha - f_\alpha^{eq})}{\rho_0}. \quad (25)$$

6. The Hybrid Computational Scheme

The mean flow field is computed using the LBE, Eq. (14), supplemented by an interpolation step, and the turbulence using the k - ϵ model transport equations. In this paper, we use the conservative formulation of the k - ϵ equations and solve them using a non-uniform *finite-volume* (FV) based scheme. The computational mesh for the k - ϵ equations is the same as that employed for the lattice grids, with each finite-volume cell centered at a lattice site, e.g. the location P shown in Fig. 3. Following the procedure in Magi^{17,18}, the discretized equations are written in *implicit* form with respect to such cells, with convective fluxes represented by an upwind scheme and the diffusive fluxes obtained using central differences across the faces, represented by the symbols N , W , S and E in Fig. 3. They are solved using the *strongly implicit procedure* (SIP) due to Stone³⁹ to obtain rapid convergence of the solutions.

7. Computational Conditions

Fluid is injected in a plane domain at a constant velocity, U_{inj} with $U_{\text{inj}}/c = 0.1$, where c is the particle speed, through a slot of width d such that $d/\delta_x = 4$, where δ_x is the minimum lattice spacing, in a relatively large closed chamber. This choice

of parameters would keep the flow in the incompressible range so that the application of the incompressible LBE model becomes valid. We consider the density of the injected fluid, ρ_0 , to be equal to 1.0. The ambient fluid, which is also of the same density, is assumed to be quiescent initially. The D2Q9 model of Fig. 1 is employed. No slip boundary conditions are imposed at the chamber walls. In this work, the boundary conditions are implemented using the non-equilibrium bounce back scheme suggested by Zou and He⁴⁰. For the k - ϵ equations, the inlet conditions are specified, based on assuming equilibrium of turbulence production and dissipation. Thus, the inlet turbulent kinetic energy and the dissipation rate are $k_{\text{in}} = 1.5u'_{\text{in}}{}^2$ and $\epsilon_{\text{in}} = k_{\text{in}}^{1.5}/l_d$ respectively. Here, u'_{in} is the root mean square value of the fluctuating component of velocity and l_d is the integral length scale. We assume $u'_{\text{in}} = 0.01U_{\text{inj}}$ and $l_d = 0.25d$. Near the walls, wall functions are used to specify the boundary conditions for the turbulent quantities³⁸. The Reynolds number of the jet, Re_d , is based on the slot width and is defined by $Re_d = U_{\text{inj}}d/\nu_{\text{lam}}$.

Two sets of problems are considered. First, to validate the LBE without a turbulence model, computations of a laminar plane jet with a Reynolds number of 12 are carried out and compared with similarity solutions. Second, we consider turbulent plane jet with Reynolds number of 3×10^4 and compare the results with measurements and with those obtained from other computational methods published in the literature. We are interested in determining the structure of the jet characterized by such quantities as the velocity distribution and the jet half-width, which will be defined in the next section. The results will be reported in terms of lattice units, i.e. the velocities are scaled by the particle velocity and the distance by the minimum lattice spacing.

8. Results and Discussion

When the injected jet travels downstream of the slot, with x as the axial distance from the slot and y as the transverse distance from the centerline of the jet, the centerline axial velocity of the jet progressively decreases as a result of diffusion of momentum along the direction transverse to the injected direction of the jet. Figure 4 shows the variation of the centerline axial velocity, $U_c(x)$, of the laminar jet, normalized by the injection velocity, U_{inj} , as a function of the axial distance from the slot, x , normalized by the slot width, d , at different times. It may be seen that the velocity distribution is transient in character. Parts of the velocity profiles, nevertheless, progressively approach steady state as time progresses. Thus, for instance, after 50,000 time steps, the centerline velocity distribution up to at least 60 slot widths downstream of the slot may be considered to be steady. Now, the analytical solution for the structure of the jet^{41,42} is applicable only for the steady part of the jet and hence they should only be used for comparison with the computed results of the steady portion of the jet. The analytical solution based on similarity considerations yields the axial velocity, $U(x, y)$, as a function of the transverse distance. It is given by the expression $U(x, y)/U_{\text{cl}} = \text{sech}^2\eta$, where $U_{\text{cl}}(x)$

is the centerline velocity and η is the similarity variable, a dimensionless coordinate given by $\eta = 0.5 (M_{\text{inj}}/6\rho_0\nu_{\text{lam}})^{1/3} y/x^{2/3}$. Here, M_{inj} is the injected momentum flow rate of the jet. The half-width of the jet, $y_{1/2}$, which is defined as the distance in the transverse direction from the centerline where $U(x, y_{1/2}) = 1/2U_{\text{cl}}(x)$, also follows from the similarity solution as $y_{1/2}/d = ARe_d^{-2/3} (x/d)^{2/3}$, where A is a constant equal to 3.2038.

Figure 5 shows the variation of the computed half-widths at different times, shown in symbols, as a function of the axial distance. Both axes are normalized by the slot width. Also plotted on the same figure is the similarity solution. It may be seen that when $t = 40,000$, at least up to 15 slot widths downstream of the slot the computed half-width profile is steady. In this range, the growth of the half-width closely agrees with the analytical solution within 4%.

The computed normalized velocity profile, $U_{\text{cl}}(x, y)/U_{\text{cl}}(x)$ as a function of the similarity velocity variable, η at 20 slot widths downstream of the jet when $t = 60,000$ is compared with the similarity profile in Fig. 6. The computed and analytical results agree within 3% for $\eta \leq 1.5$, but the differences increase at distances greater than this, due to wall effects.

Figure 7 shows the lattice/finite-volume mesh employed for the turbulent jet computations. A nominal resolution with 400 lattice grids in both the axial and transverse directions are employed. The grids are spaced non-uniformly with stretching applied in both the directions. The mesh is considered to be uniform in the near-field region of the slot, where strong gradients in the flow field is expected. Effectively, the mesh accommodates a rectangular domain, whose length in the axial distance equals $475d$ and that in the transverse direction equals $270d$.

Figure 8 shows the velocity vector field in the domain of the turbulent jet after 10,000 time steps. Also shown in the same figure is a plot representing the velocity vector field in the near-field of the slot. It may be seen that a pair of vortices, the starting vortex or the head vortex pair, are formed from the two shear layers of the injected jet and the ambient fluid. As time progresses, it was observed that these vortices convect downstream along with the unsteady part of the jet. Also seen in the figure is the potential core, in which the jet preserves the injected velocity for certain distance downstream from the slot. These basic feature of the jet are consistent with those observed in experiments and in the numerical simulations based on the Navier-Stokes equations.

The computed axial velocity profile, normalized by the centerline velocity, is plotted as a function of the transverse distance normalized by the jet half-width at 20 slot widths downstream of the slot for different times in Fig. 9. It is well known that the steady part of the transient jet exhibits asymptotic self-similarity after a certain distance downstream of the slot. It may be seen that at the downstream location plotted in Fig. 9, the velocity profiles at different times almost overlap with one another, implying steady state there. Shown on the same plot in symbols are the data from the measurements by Gutmark and Wygnanski⁴³. The computed

results agree within 10% with the measured values.

As a consequence of self-similarity, the axial variation of the centerline velocity and the half-width of the jet obey the following scaling laws⁴²: $U_{cl}(x) \sim x^{-1/2}$ and $y_{1/2}(x) \sim x$. Thus, in the region of self-similarity, $(U_{inj}/U_{cl}(x))^2$ should be a linear function of the axial distance, x . Figure 10 shows the computed values of $(U_{inj}/U_{cl}(x))^2$, in filled circles, as a function of the normalized axial distance after 80,000 time steps. It may be seen that the computed results indeed follow a linear variation as expected and agree qualitatively with the measurements. Quantitatively, the data may be fitted to a linear curve that may be represented by

$$\left(\frac{U_{inj}}{U_{cl}(x)}\right)^2 = C_1 \left[\frac{x}{d} + C_2\right]. \quad (26)$$

In this work, this linear curve fit is applied to the computed results for the range of distances given by $20 \leq x/d \leq 140$ and the constants C_1 and C_2 thus obtained are reported in Table 1, where data from other sources are also compiled for comparison. The sources include the three measurements noted above and the direct numerical simulation (DNS) data by Stanley *et al.*⁴⁶ and the large eddy simulation (LES) results by Le Ribault *et al.*⁴⁷ It may be seen that there is a considerable scatter in the values of the constants. In particular, the constant C_2 which represents the intercept of the linear fit vary significantly, which predominantly reflects the quantitative difference between the computed variation and the measurement by Gutmark and Wygnanski⁴³. Physically, this constant is associated with the location of the *virtual origin* of the jet and hence it is expected that different methods could result in different values of this constant.

Figure 11 shows the computed normalized half-width, in filled circles, plotted as a function of the normalized axial distance. It may be seen that the computed results show a linear trend consistent with the similarity scaling law. For a quantitative comparison, the results are fitted according to the following linear curve

$$\left(\frac{y_{1/2}}{d}\right) = K_1 \left[\frac{x}{d} + K_2\right]. \quad (27)$$

The constants K_1 and K_2 are presented in Table 1. The slope of this curve, i.e. $dy_{1/2}/dx$ or K_1 is referred to as the *spreading rate* of the jet and is a constant in the similarity region. It is important to reproduce this quantity with sufficient accuracy in engineering applications, as it is one of the measures of the rate of mixing of the injected and the ambient fluids. In Table 1, along with the computed spreading rate, the spreading rate based on the *steady* Reynolds averaged Navier-Stokes (RANS) equations with different two-equation models as reported by Wilcox³³ and also by Magi *et al.*⁴⁸ based on the *unsteady* RANS equations with the standard $k-\epsilon$ are presented. The measured values for this quantity are in the range 0.100 – 0.110. The values based on the direct numerical simulation (DNS) and that based on the turbulence models, including the large eddy simulation (LES) turbulence models, are in the range 0.090–0.110. The computed value based on the LBE/ $k-\epsilon$ FV scheme

yields a value for the spreading rate as 0.0965 which is within 5% agreement with these other studies.

9. Summary and Conclusions

In this paper, it is shown that the LBE with a spatially and temporally dependent relaxation time paper follows *á priori* from its continuous version. Computations of transient incompressible turbulent plane jets are reported by employing this LBE in conjunction with the standard k - ϵ turbulence model equations. The turbulence transport equations are solved using a finite-volume (FV) scheme on non-uniform grids. The computed structure of the turbulent jet is shown to be consistent with prior measurements and computed results. In particular, this hybrid LBE-FV k - ϵ scheme is found to reproduce the similarity scaling laws for turbulent jets, i.e., the $x^{-1/2}$ decay for the centerline jet velocity and linear growth of the jet half-width. The computed results agree with the measurements to within 10%. Laminar jet computations are shown to be in agreement with the analytical solution. Although not shown here, we have shown elsewhere⁴⁹ that this hybrid approach is computationally more efficient on parallel computers as compared to the conventional schemes¹⁹ when its inherent parallelism is exploited.

References

1. U. Frisch, B. Hasslacher, and Y. Pomeau *Phys. Rev. Lett.* **56**, 1505 (1986).
2. S. Wolfram, *J. Stat. Phys.* **45**, 471 (1986).
3. G.R. McNamara and G. Zanetti, *Phys. Rev. Lett.* **61**, 2332 (1988).
4. Y. Qian, D.d'Humières and P. Lallemand, *Europhys. Lett.* **17**, 479 (1992).
5. H. Chen, S.Chen, D. Martinez and W. Matthaeus, *Phys. Rev. Lett.* **67**, 3776 (1991).
6. P.L. Bhatnagar, E.P. Gross and M. Krook, *Phys. Rev.* **94**, 511 (1954).
7. X. He and L.-S. Luo, *Phys. Rev.E* **55**, R6333 (1997).
8. X. He and L.-S. Luo, *Phys. Rev.E* **56**, 6811 (1997).
9. T. Abe, *J. Comp. Phys.* **131**, 241 (1997).
10. R. Benzi, S. Succi and M.V. Vergasola, *Phys. Rep.* **222**, 147 (1992).
11. Y.H. Qian, S. Succi and S.A. Orszag, *Annu. Rev. Comp. Phys.* **3**, 195 (1995).
12. S. Chen and G.D. Doolen, *Annu. Rev. Fluid. Mech.* **30**, 329 (1998).
13. S. Succi, O. Filippova, G. Smith and E. Kaxiras, *Comput. Sci. Eng.* **36**, 26 (2001).
14. S. Succi, I.V. Karlin and H. Chen, *Rev. Mod. Phys.* **74**, 1203 (2002).
15. D. Wolf-Gladrow, *Lattice-Gas Cellular Automata and Lattice Boltzmann Models, Lecture Notes in Mathematics, No. 1725* (Springer, New York, 2000).
16. S. Succi, *The Lattice Boltzmann Equation for Fluid Dynamics and Beyond* (Oxford University Press, 2001).
17. F. Grasso and V. Magi, in *Numerical Simulation of Combustion Phenomena, Lecture Notes in Physics* **241**, 282 (1985).
18. F. Grasso and V. Magi, in *Modern Research Topics in Aerospace Propulsion*, ed. G. Angelino, L. De Luca and W.A. Sirignano (Springer-Verlag, 1991), p. 227.
19. K. N. Premnath, V. Magi and J. Abraham, in *Grand Challenges in Computer Simulations — Proc. High Perf. Comput. Symp.*, ed. A. Tentner (San Diego, CA, 2002), p. 3.

20. S. A. Orszag and V. Yakhot, *Phys. Rev. Lett.* **56**, 1691 (1986).
21. D.O. Martinez, W. Matthaeus, S. Chen and D. Montgomery, *Phys. Fluids* **6**, 1285 (1994).
22. R. Benzi and S. Succi, *J. Phys. A: Math. Gen.* **23**, L1 (1990).
23. R. Benzi, M.V. Struglia and R. Tripiccone, *Phys. Rev. E* **53**, R5565 (1996).
24. G. Amati, S. Succi and R. Benzi, *Fluid Dyn. Res.* **19**, 289 (1997).
25. V.V. Aristov, in *Proc. 21st Int. Symp. Rarefied Gas Dynamics*, ed. R. Brun (Marseille, 1999), p. 187.
26. A. Sakurai and F. Takayama, *Phys. Fluids* **15**, 1282 (2003).
27. H. Chen, S. Succi and S. A. Orszag, *Phys. Rev. E* **59**, R2527 (1998).
28. S. Succi, A. Amati and R. Benzi, *J. Stat. Phys.* **81**, 5 (1995).
29. S. Hou, J. Sterling, S. Chen and G.D. Doolen, *Field Inst. Comm.* **6**, 151 (1996).
30. C. Teixeira, *Int. J. Mod. Phys. C* **9**, 1159 (1998).
31. S. Chapman and T.G. Cowling, *Mathematical Theory of Non-Uniform Gases* (Cambridge University Press, 1964).
32. O. Filippova, S. Succi, F. Mazzocco, C. Arrighetti, G. Bella and D. Hanel, *J. Comp. Phys.* **170**, 812 (2001).
33. D. C. Wilcox, *Turbulence Modeling for CFD* (DCW Industries, CA, 1998).
34. J. Abraham, *SAE Trans.* **106**, 147 (1997).
35. X. He and L.-S. Luo, *J. Stat. Phys.* **88**, 927 (1997).
36. X. He, L.-S. Luo and M. Dembo, *J. Comp. Phys.* **129**, 357 (1996).
37. X. He, *Int. J. Mod. Phys. C* **8**, 737 (1997).
38. B.E. Launder and D.B. Spalding, *Comput. Meth. Appl. Mech. and Engg.* **3**, 269 (1974).
39. H. L. Stone, *SIAM J. Numer. Anal.* **5**, 530 (1968).
40. Q. Zuo and X. He, *Phys. Fluids* **4**, 1510 (1997).
41. W. G. Bickley, *Phil. Mag.* **23**, 727 (1937).
42. H. Schlichting, *Boundary Layer Theory* (McGraw-Hill, New York, 1976).
43. E. Gutmark and G. Wygnanski, *J. Fluid Mech.* **73**, 465 (1976).
44. L.W.B. Browne, R.A. Antonia, S. Rajagopalan and A.J. Chambers, in *Structure of Complex Turbulent Shear Flow — Proc. IUTAM Symp.*, ed. R. Dumas and L. Fulachier (Marseille, 1982), p. 411.
45. F.O. Thomas and H.C. Chu, *Phys. Fluids A* **1**, 1556 (1989).
46. S.A. Stanley, S. Sarkar and J.P. Mellado, *J. Fluid Mech.* **450**, 377 (2002).
47. C. Le Ribault, S. Sarkar and S.A. Stanley, *Phys. Fluids* **11**, 3069 (1999).
48. V. Magi, V. Iyer and J. Abraham, *Numer. Heat Transfer Part A* **40**, 317 (2001).
49. K. N. Premnath and J. Abraham, in *Grand Challenges in Computer Simulations — Proc. High Perf. Comput. Symp.*, ed. A. Tentner (San Diego, CA, 2002), p. 49.

Table 1. Comparison of the coefficients of the fitted linear curve for the normalized inverse square axial velocity and the normalized axial variation of the half-width of the turbulent jet.

Source	Re_d	C_1	C_2	K_1	K_2
LBE / Std. $k - \epsilon$ model - this work	30,000	0.1371	0.0607	0.0965	-0.488
Unsteady RANS / Std. $k - \epsilon$ model ⁴⁸	—	—	—	0.103	—
Steady RANS / Std. $k - \epsilon$ model ³³	—	—	—	0.108	—
Steady RANS / Std. $k - \omega$ model ³³	—	—	—	0.101	—
LES/dynamic Smagorinsky SGS model ⁴⁷	3,000	0.100	0.89	0.094	1.38
LES/dynamic mixed SGS model ⁴⁷	3,000	0.220	0.18	0.106	0.40
DNS ⁴⁶	3,000	0.201	1.23	0.092	2.63
Measurement - Thomas & Chu (1989) ⁴⁵	8,300	0.220	-1.19	0.110	0.14
Measurement - Browne <i>et al.</i> (1983) ⁴⁴	7,620	0.143	-9.00	0.104	-5.00
Measurement - Gutmark & Wygnanski(1976) ⁴³	30,000	0.123	4.47	0.100	-2.00

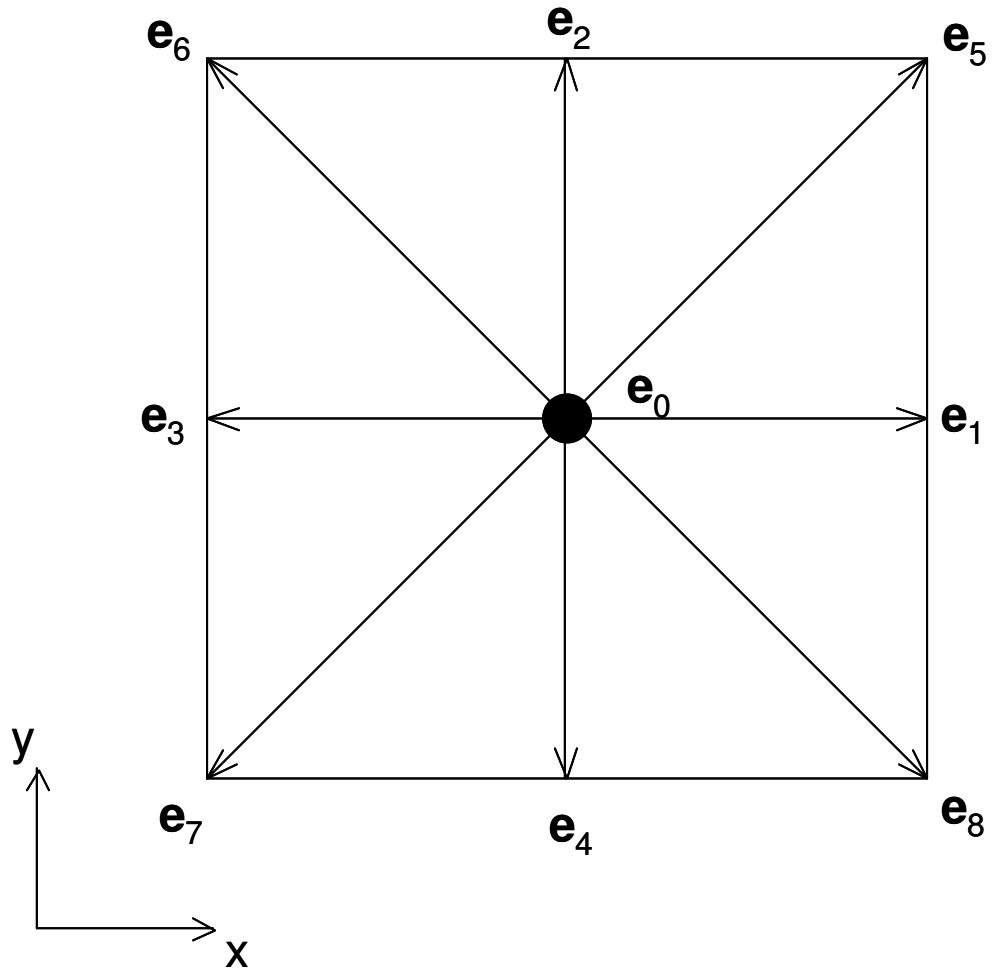


Fig. 1. D2Q9 Lattice.

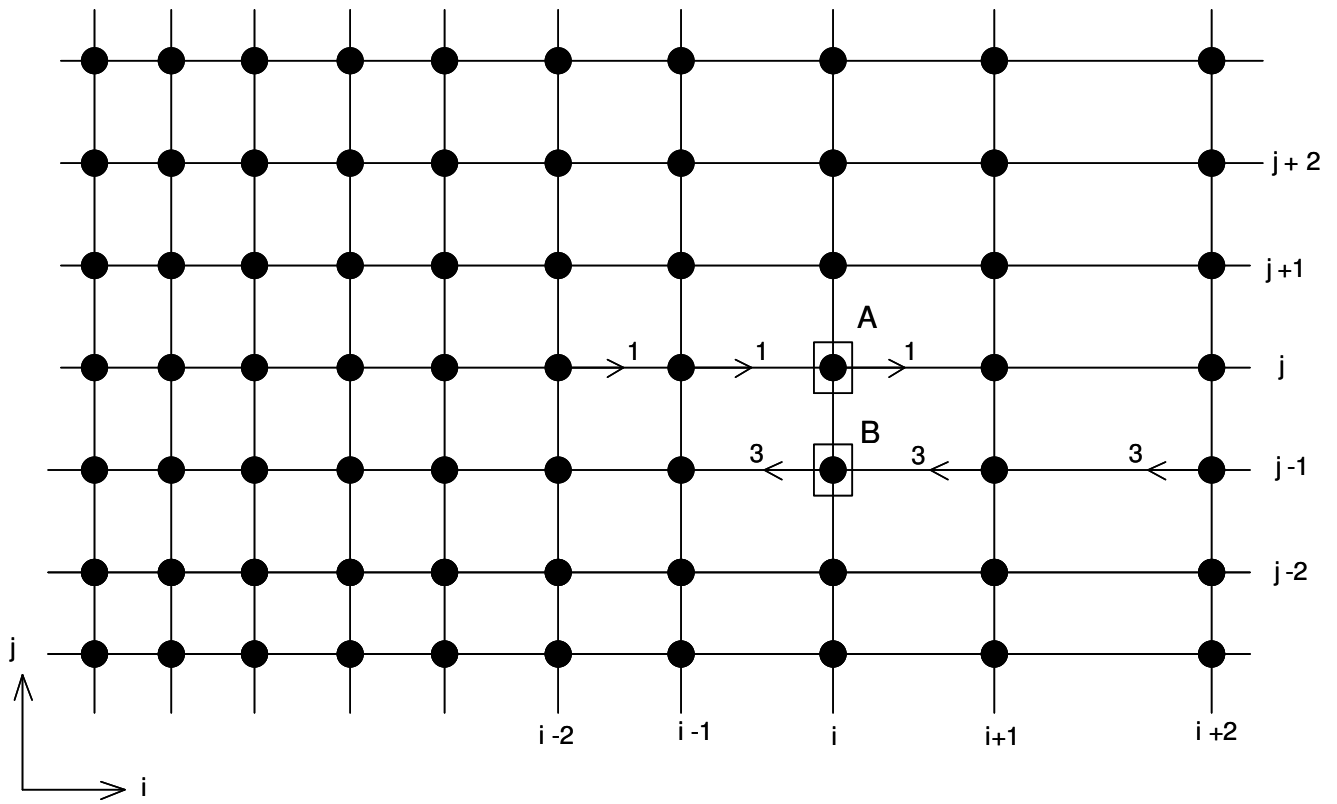


Fig. 2. Non-uniform lattice mesh.

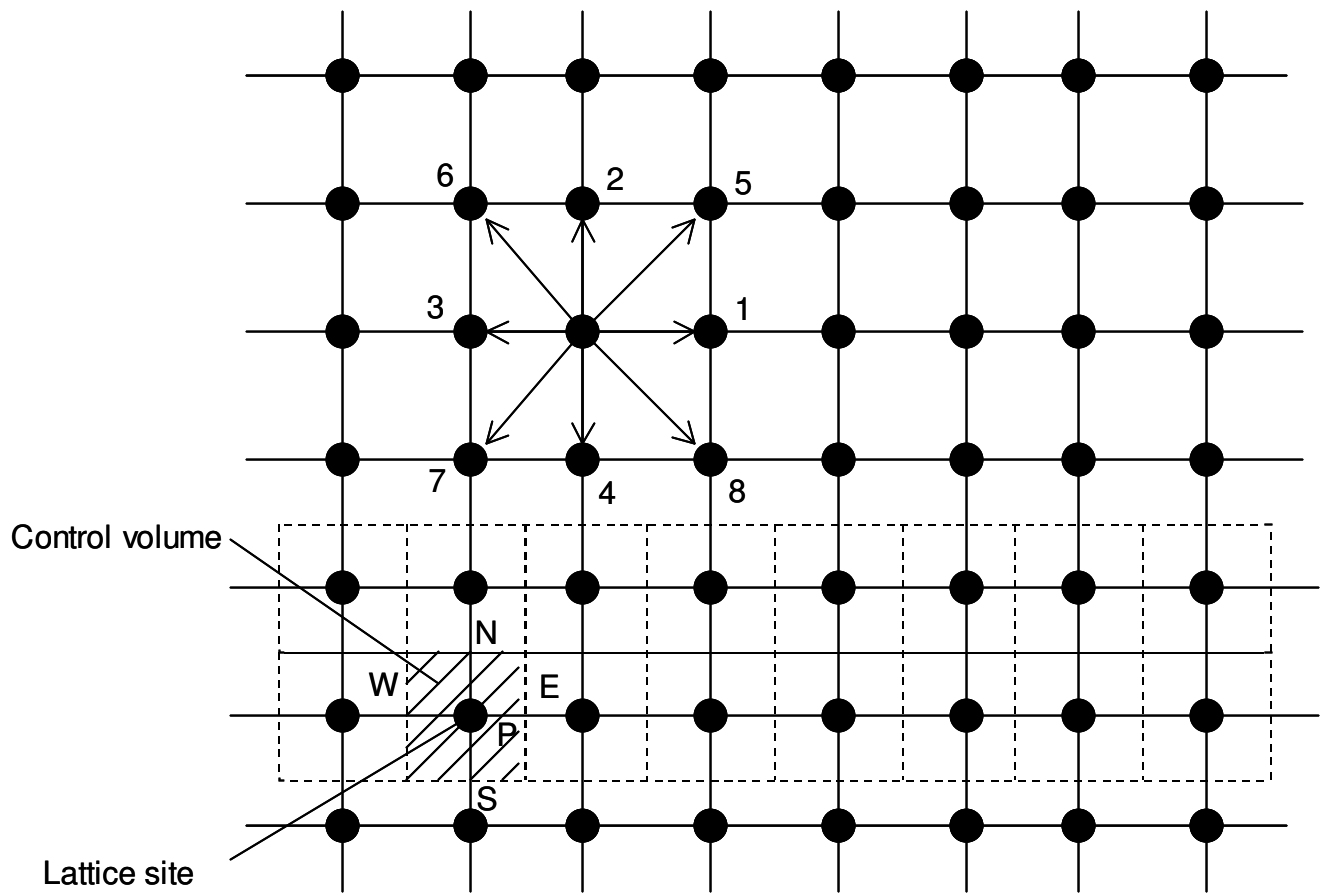


Fig. 3. Finite control volumes embedded on lattice mesh.

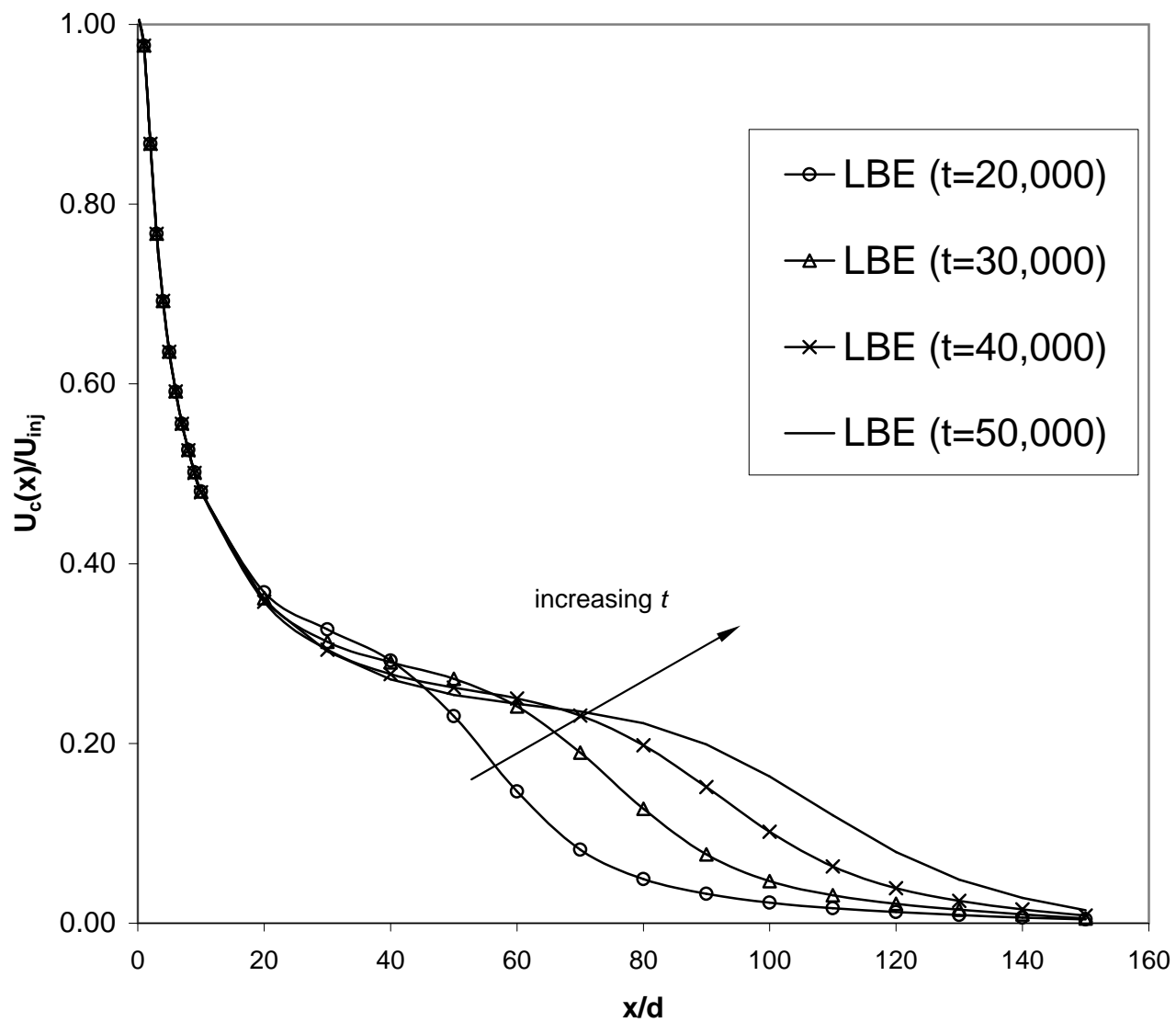


Fig. 4. Transient axial velocity profiles as a function of axial distance of the laminar jet; $Re_d = 12$.

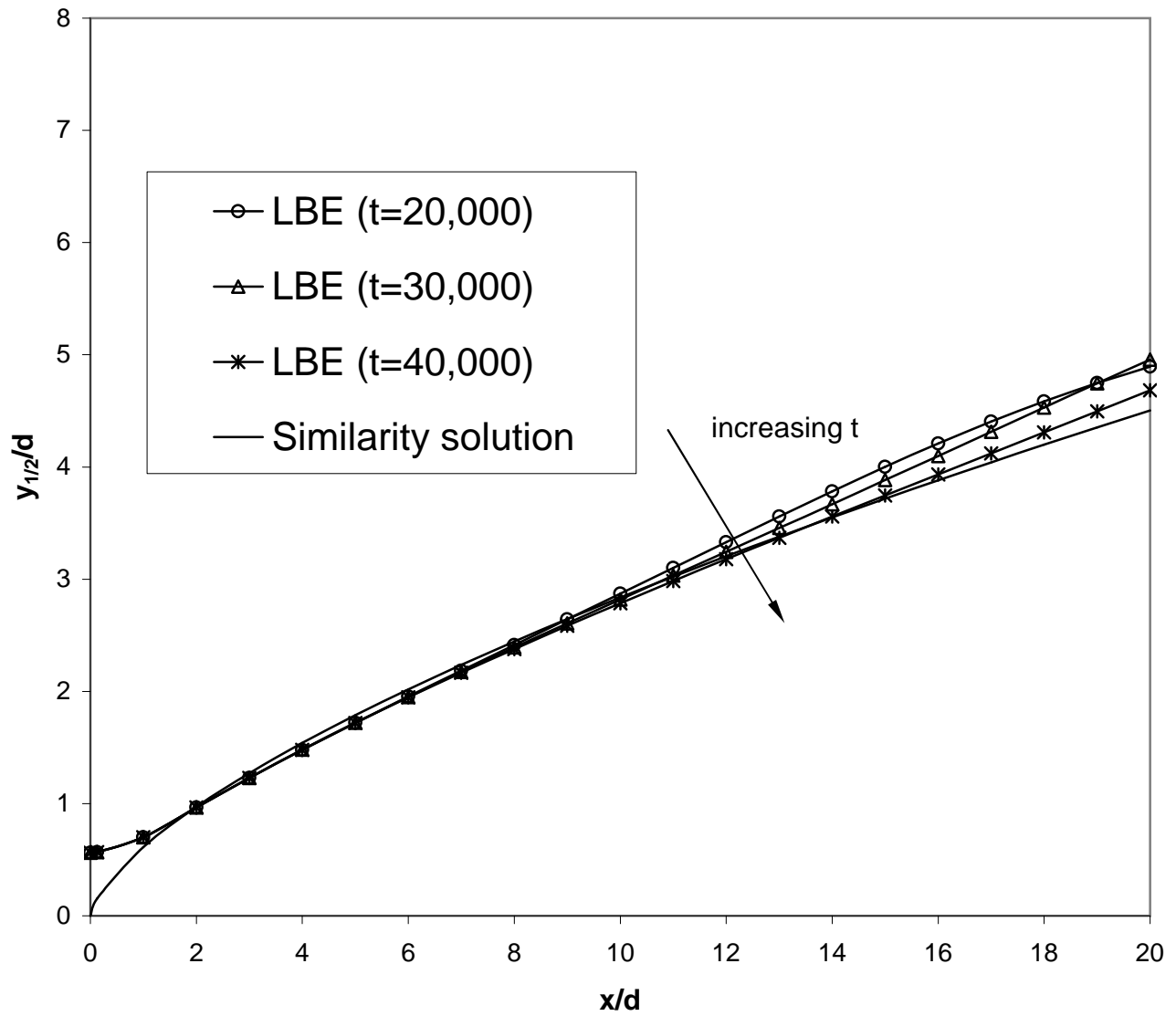


Fig. 5. Comparison of computed results and similarity solution⁴¹ for half-width of the laminar jet; $Re_d = 12$.

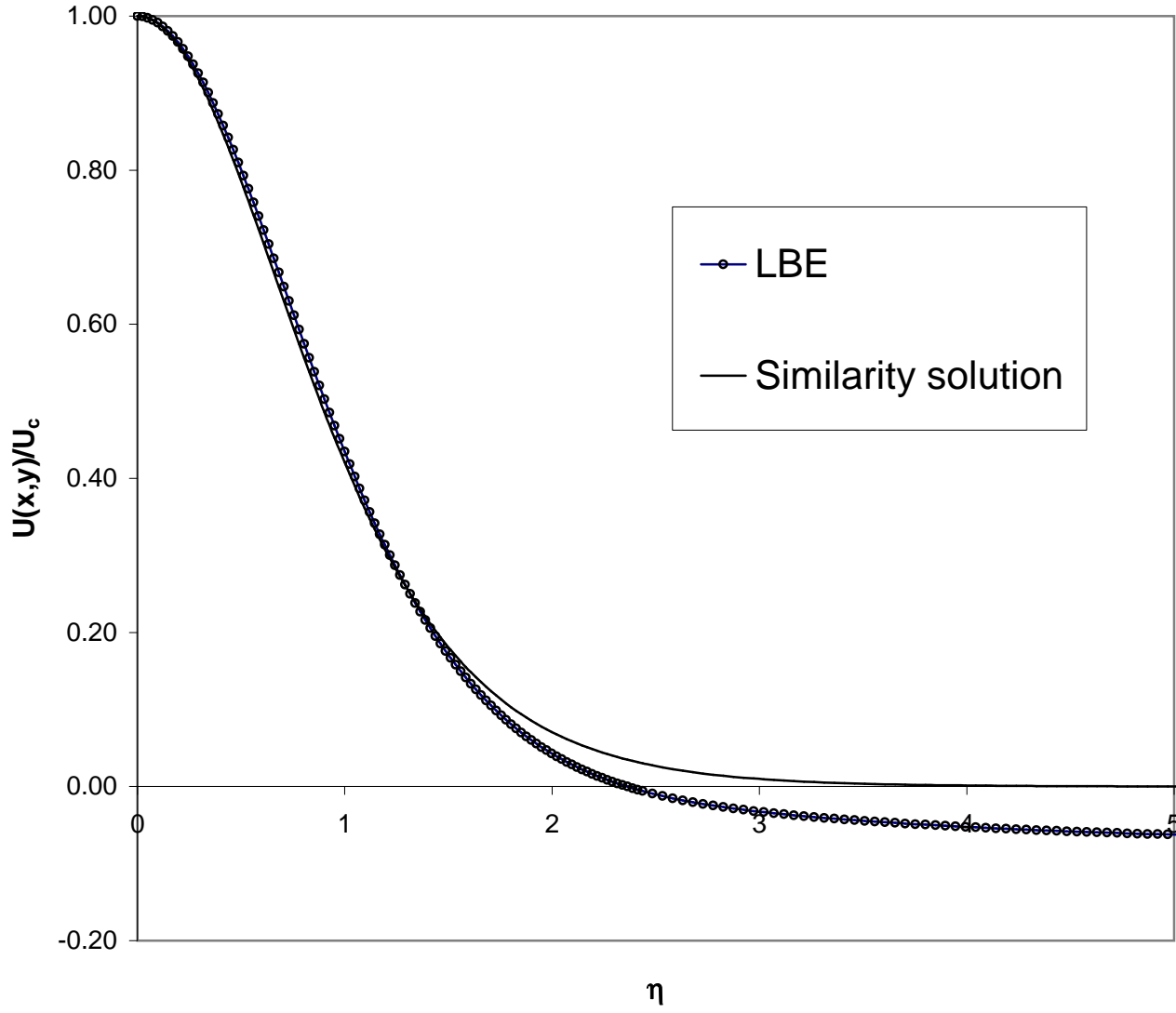


Fig. 6. Comparison of computed results and similarity solution⁴¹ for the normalized axial velocity as a function of similarity variable of the laminar jet; $Re_d = 12$, $x/d = 20$.

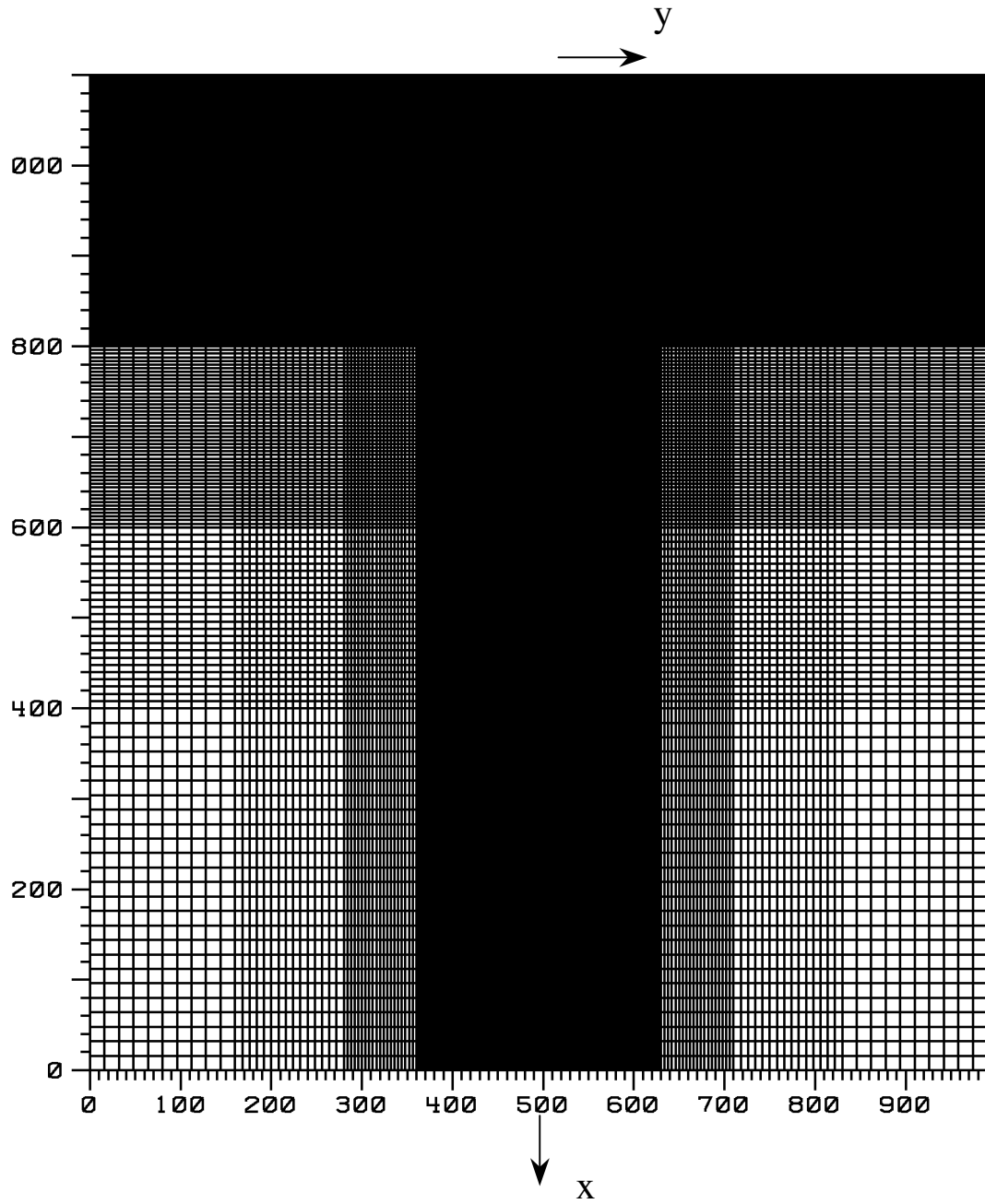


Fig. 7. Computational lattice/finite volume mesh employed.

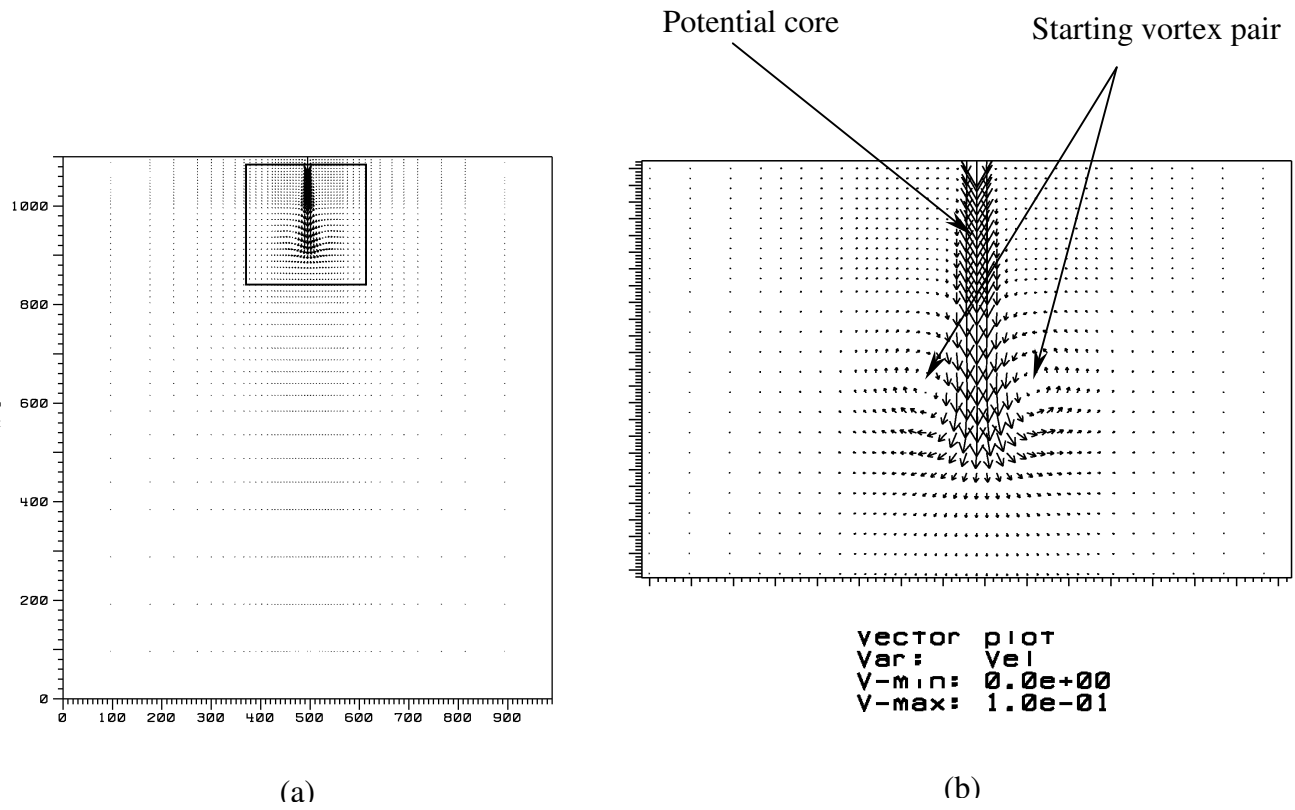


Fig. 8. (a) Velocity vector field in the domain of the turbulent jet after 10,000 time steps; (b) Velocity vector field in the near-field of the slot showing the potential core and the starting vortex pair; $Re_d = 30 \times 10^4$.

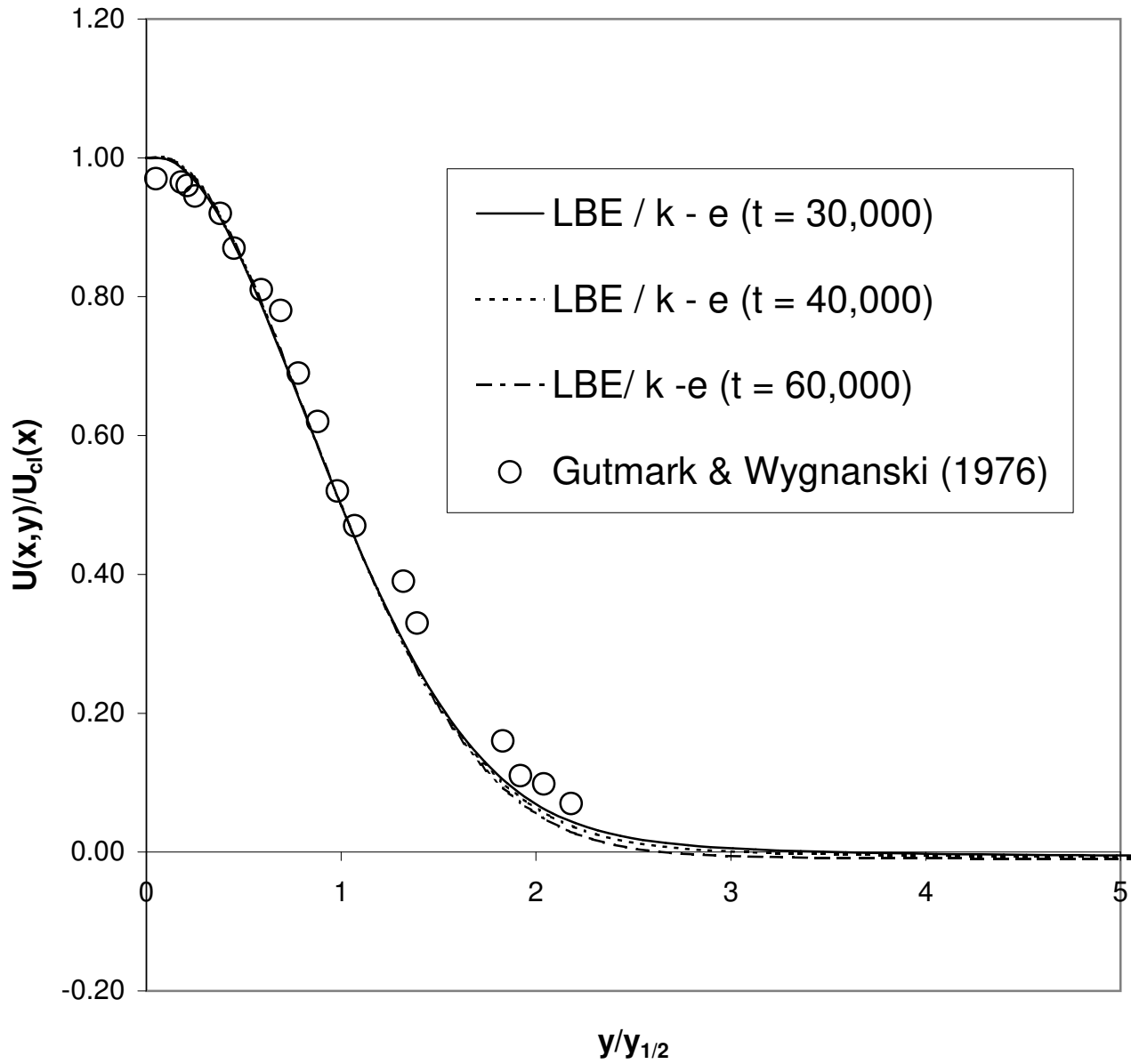


Fig. 9. Comparison of computed results and measurements for the normalized axial velocity profile as a function of the similarity variable of the turbulent jet; $Re_d = 30 \times 10^4$, $x/d = 20$.

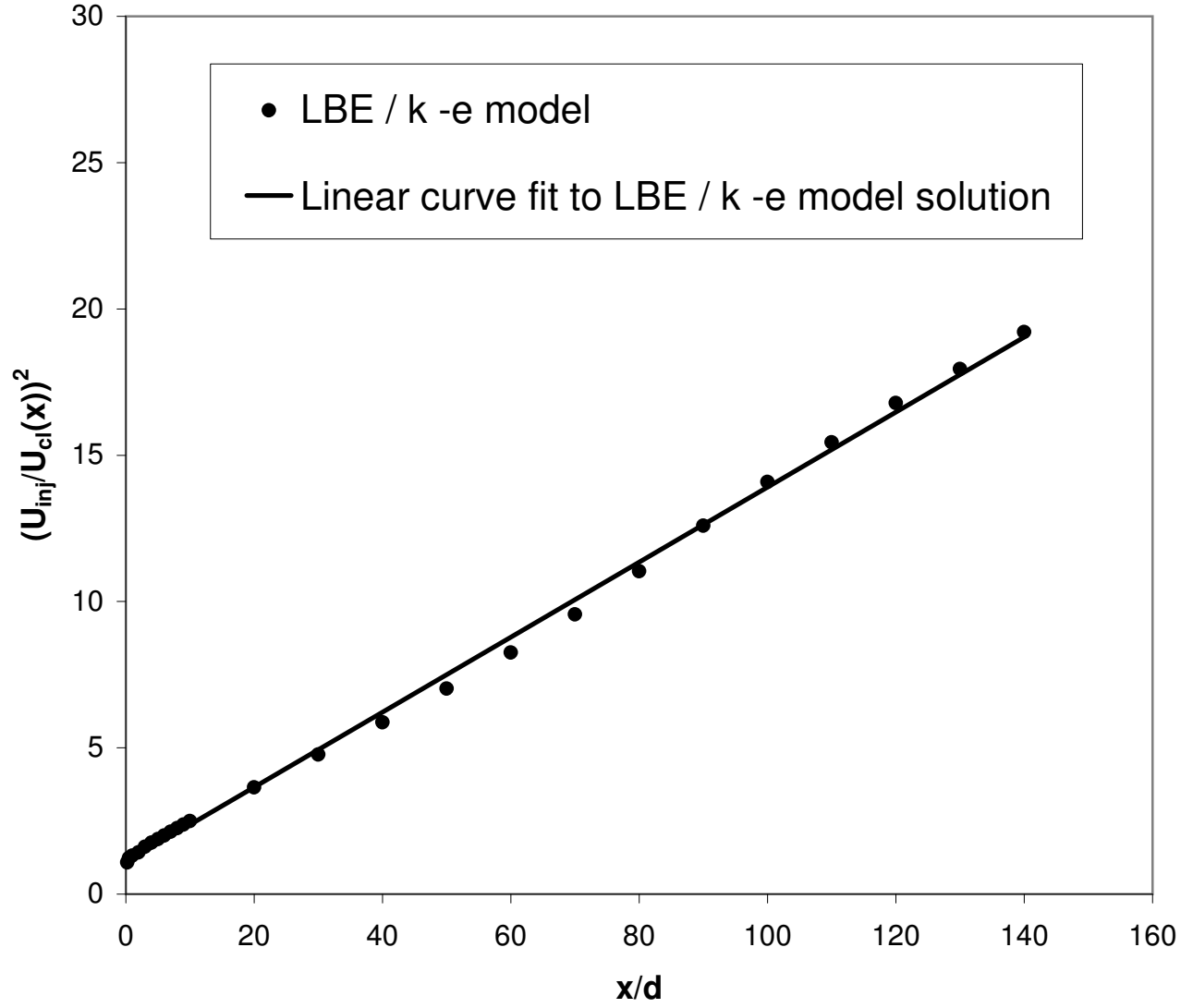


Fig. 10. Normalized inverse square of the centerline velocity as a function of the normalized axial distance of the turbulent jet; $Re_d = 30 \times 10^4$.

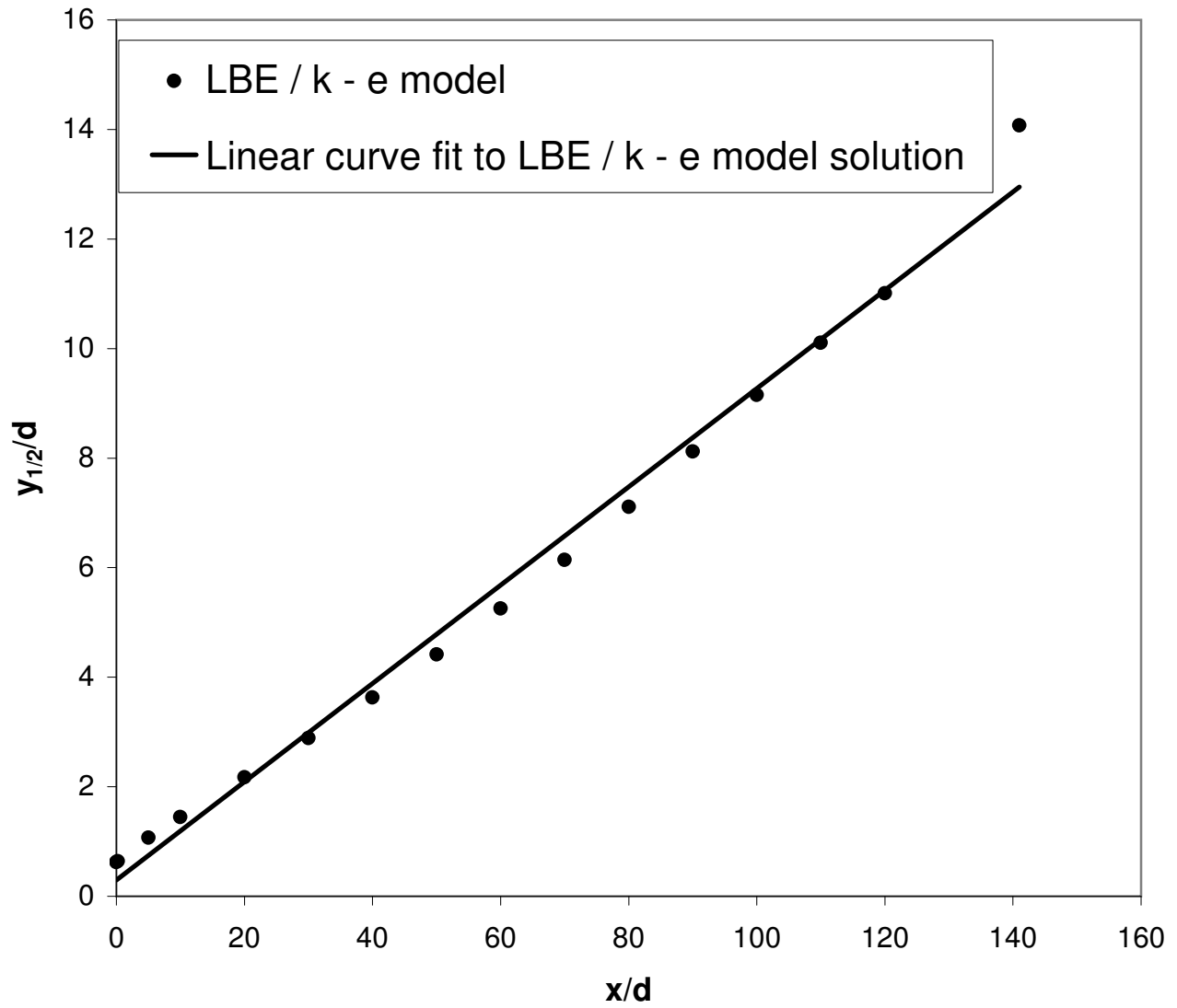


Fig. 11. Normalized jet half-width as a function of the normalized axial distance of the turbulent jet; $Re_d = 30 \times 10^4$.